Petroleum Science 23 (2026) 2435–2451

Contents lists available at ScienceDirect

Petroleum Science

journal homepage: www.keaipublishing.com/en/journals/petroleum-science

Original Paper

A model for shale gas flow and permeability leveraging coupled transport mechanisms

Shuai Chen [a], Fu-Shen Liu [b,*], Feng-Gang Wen [c], Hong-Fei Duan [d,e], Xu-Lin Peng [f]

[a] Institute of Mathematics, Henan Academy of Sciences, Zhengzhou, 450046, Henan, China
[b] Research Center of Coastal and Urban Geotechnical Engineering, Zhejiang University, Hangzhou, 310058, Zhejiang, China
[c] Shaanxi Key Laboratory of Lacustrine Shale Gas Accumulation and Exploitation, Xi'an, 710065, Shaanxi, China
[d] School of Civil Engineering, Sun Yat-sen University, Zhuhai, 519000, Guangdong, China
[e] State Key Laboratory for Tunnel Engineering, Sun Yat-sen University, Guangzhou, 510275, Guangdong, China
[f] School of Mathematical Sciences, Soochow University, Suzhou, 215006, Jiangsu, China

ARTICLE INFO

Article history:
Received 8 October 2025
Received in revised form
26 December 2025
Accepted 7 March 2026
Available online 12 March 2026

Edited by Xiu-Fang Hu

Keywords:
Shale gas
Apparent permeability
Molecule counts
Effective pressure
Adsorption
End effects

ABSTRACT

The extraction of shale gas is challenged by complex flow mechanisms and significant microscale effects within nanoscale pores. Existing models often overlook key flow mechanisms such as end effects, leading to limited predictive accuracy. To address this, we develop a novel capillary-based apparent permeability model that innovatively weights continuum flow and Knudsen diffusion according to the proportion of molecule counts in each flow region. Surface diffusion is further linearly superposed to establish a comprehensive permeability model. Most importantly, this model integrates, for the first time, the effects of effective pressure, adsorption, end effects, real gas effects, and confinement effects. The proposed model is validated against published experimental data under both constant effective pressure and constant confining pressure, showing superior agreement compared to existing theoretical models. Sensitivity analysis reveals that neglecting end effects and surface diffusion leads to underestimation of permeability, while overlooking effective pressure results in overestimation. The influence of each mechanism varies distinctly with pore radius: surface diffusion and real gas effects dominate in smaller pores ($\leq$10 nm), whereas end effects become predominant in larger pores ($\geq$25 nm). This work provides a more reliable theoretical foundation for predicting shale gas permeability and optimizing extraction strategies.

1. Introduction

With declines in conventional oil and gas resources, unconventional resources such as shale gas have gradually become a focal point of research (Chen et al., 2025; Zhu et al., 2025). Shale reservoirs are characterized by features such as low porosity and low permeability (Arif et al., 2017; Pan et al., 2018), and thus, efficient extraction of their resources remains a significant challenge. In shale reservoirs, pore size predominantly ranges from 4 nm to 200 nm, exhibiting multiscale characteristics. Meanwhile, gas exists in such reservoirs in three states: dissolved, adsorbed, and free gas. The complexity of gas transport regimes is therefore attributed to the diversity of these storage modes and the multiscale structure (Hatami et al., 2020). Among them, a well-known manifestation of rarefaction in gas microflows is the Knudsen layer, a zone of local non-equilibrium adjacent to the wall with a thickness on the order of a few mean free paths, as shown in Fig. 1. Permeability serves as a pivotal parameter for quantifying extraction efficiency, the magnitude of which is influenced by factors including transport regimes, effective pressure, adsorption, and others. Consequently, the focus of this work is on constructing a more rational and accurate model for shale apparent permeability.

There are currently three methods for testing permeability: experimental measurement, numerical simulation, and analytical modeling. In experimental measurements, the velocity of gas flow is markedly slow, and this limitation is compounded by the intricate procedure required for sample preparation; therefore, a degree of variance is observed in test results of identical samples

* Corresponding author.
E-mail address: fushenliu@zju.edu.cn (F.-S. Liu).
Peer review under the responsibility of China University of Petroleum (Beijing).

https://doi.org/10.1016/j.petsci.2026.03.013

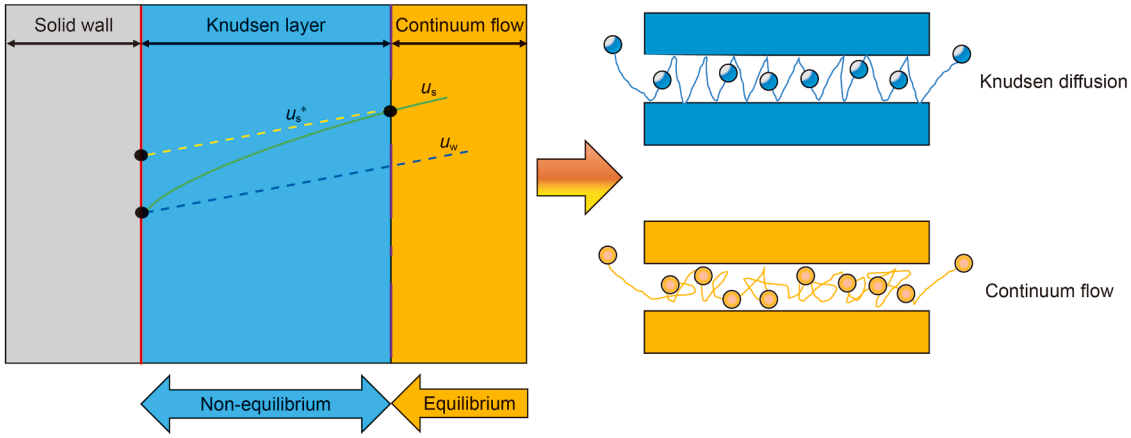

Fig. 1. Schematic of the Knudsen layer structure near a wall in a gas microflow, comparing the actual velocity profile (solid line) with the continuum-based models' prediction (dashed lines) (u_s^*: N–S velocity; u_s: actual velocity; u_w: wall velocity) (Watari, 2010).

across different experiments (Darabi et al., 2012). Numerical simulation is a methodology that employs computer programs to find solutions in mathematical models (Javadpour et al., 2021). Among these methodologies, molecular dynamics simulation stands out as a particularly promising approach, offering a refined and detailed perspective for investigating fluid-surface interactions and associated chemical phenomena over the years (Velioglu and Keskin, 2019; Xiong et al., 2020; Yu et al., 2018). It is noteworthy that in the field of petroleum engineering, the application of molecular dynamics simulation has consistently been constrained by its characteristic of generating large-scale datasets, which has somewhat limited the widespread adoption of this method (Ma et al., 2024). In addition to molecular dynamics simulation, machine learning is rapidly emerging as a pivotal technology in petroleum engineering (Ma et al., 2024). Indeed, the deep integration of machine learning principles with petroleum engineering practices has already yielded significant impacts and will continue to drive critical advancements in the field. At the micro- and nano-scales, machine learning technologies have demonstrated marked advantages in characterizing fluid flow and fluid–rock interactions, offering a powerful new tool for advancing fundamental understanding and optimizing related processes efficiently. Machine learning models offer an effective approach for predicting the permeability of rocks and granular materials, which is essential for accurately characterizing fluid flow behavior in porous media. Currently, there is a growing trend toward integrating molecular-dynamics-generated data using machine learning techniques. Although molecular dynamics simulation and machine learning have both been widely applied in petroleum engineering, systematic studies integrating the two approaches remain relatively scarce. Current literature primarily focuses on their synergistic use in fields such as chemistry (Gasteiger and Zupan, 1993; Wang et al., 2019), biology (Wang et al., 2020), materials science (Noé et al., 2020), and physics (Bartók et al., 2010; Behler, 2016), while cross-disciplinary exploration within petroleum engineering is still limited.

In contrast, analytical models can deliver precise computational results, and they enable better understanding of the impact of model parameters, making them the prevailing choice in the current research landscape (Akilu et al., 2021). In shale reservoirs, the internal pores exhibit significant heterogeneity and tortuosity. This heterogeneity increases the flow resistance of the gas, making the flow behaviors of shale gas extraordinarily complex. Several studies have explored analytical models for shale permeability, and among them, the Navier-Stokes equation is frequently employed to characterize continuum flow, operating under the assumption that the fluid is continuous and indivisible (Gad-el-Hak, 2003). However, various transport regimes coexist in shale pores, each requiring distinct mathematical models for characterization; thus, it is essential to establish an analytical model that encompasses all flow regimes. Based on this, researchers have developed two distinct classes of analytical models: one class is rooted in the continuum flow equation, incorporating a slip boundary to describe various transport regimes, and the other employs superposition of different transport regimes. During gas flow in shale reservoirs, the slip effect is frequently observed. In 1941, Klinkenberg introduced an empirical slip model based on experimental observations. However, its applicability is limited as it exclusively addresses slip flow (Klinkenberg, 1941). Subsequently, Beskok and Karniadakis (1999) derived a gas transport equation in a single straight capillary based on dimensional analysis; building on this theoretical framework, Civan (2010) utilized the numerical solution of the linear Boltzmann equation to obtain a corrected, more streamlined formula. This general slip boundary condition is distinct from the Maxwell boundary condition, as it surpasses the limitation of a Knudsen number of "1". Although this broadens its scope of application, this method is not derived from fundamental theoretical analysis. The other approach is the superposition of different transport regimes. Javadpour (2009) formulated a gas transport equation through the linear superposition of slip flow and Knudsen diffusion, introducing the concept of "apparent permeability" in the realm of unconventional shale gas migration. Later on, a permeability model was developed by Wu et al. (2015a, 2017), utilizing slip flow and Knudsen diffusion in combination with weight coefficients. These models often overlook the impacts of key mechanisms such as surface diffusion, confinement effects, real gas effects, effective pressure, and adsorption, which introduce inaccuracies in model predictions.

Through detailed investigations of shale microstructure and transport regimes, previously obscure transport regimes have been uncovered which can be crucial in specific conditions. During shale gas extraction, alterations in the stress environment induce modifications in the pore structure, and therefore it is imperative to account for the effects brought about by variations in pore size. Effective pressure and adsorption are the predominant factors driving these pore size alterations. In terms of adsorption, it influences gas flow in two significant ways. First, adsorbed gas

constitutes a substantial proportion of the total gas (Yu et al., 2017); a large quantity of adsorbed gas is a main factor leading to reduced extraction efficiency. Second, the effect of sorption-induced strain leads to a reduction in the effective pore volume, resulting in a decrease in the amount of transport channels (Cao et al., 2016). Consequently, it is vital to consider adsorption in the permeability modeling process for shale gas flow. Additionally, as the pore pressure decreases, the effective pressure increases, leading to reductions in pore size and permeability (Tan et al., 2018; Wang et al., 2018a). In real extraction environments, the reduction of pore pressure leads to the transformation of a significant amount of adsorbed gas into free gas, resulting in an increase in pore size; concurrently, the increase in effective pressure leads to pore closure. This analysis indicates that permeability is constrained by the combined effects of effective pressure and adsorption (Peng et al., 2018). While significant focus is placed on behaviors within shale pores, the influence of gas flow behaviors at the inlet and outlet of the channels is often overlooked, leading to less accurate and less precise model predictions. For transport channels of finite length, previous calculations of flow rate have solely focused on channel interiors. However, at the inlets and outlets of the channels, highly viscous shear zones exist, leading to a loss in flow rate – these are known as "end effects" (Sisan and Lichter, 2011; Weissberg, 1962). When we neglect such end effects, the pressure loss at the inlet and outlet is attributed to the internal pressure loss, rendering us unable to accurately predict the permeability. Shale gas transport is not only driven by pressure gradients but is also influenced by colloidal forces, such as the real gas effect and confinement effect (Sun et al., 2018). Because of the real gas effect and confinement effect, the gas thermodynamic properties diverge from those of bulk gas, and thus these factors are crucial to include in permeability modeling. Due to the complex pore structure of shale, Si et al. (2018) have proposed utilizing capillary models to simplify the structure — an approach which has been recognized for its structural simplicity and computational convenience. Building on this, other researchers have integrated multiple transport mechanisms and microscale effects into capillary models. Several of these models have been experimentally validated, demonstrating a degree of reliability in characterizing unconventional shale gas flow (Cai et al., 2018; Si et al., 2018, 2019; Zhu et al., 2018). Overall, the confinement effect, real gas effect, surface diffusion, effective pressure, adsorption, and end effects are indispensable factors influencing permeability. However, existing models have not comprehensively accounted for these elements.

Although significant advancements have been made regarding shale permeability models, prior research has often overlooked the impact of certain key mechanisms and is unable to fully capture the transport behaviors of shale gas. In light of this, we delineate different transport regimes in a novel capillary model for shale permeability. Specifically, the proportions of molecule counts in different areas relative to the total molecule counts are utilized as weighting coefficients to couple continuum flow and Knudsen diffusion, while also considering surface diffusion driven by concentration gradients. Building on this foundation and considering the unique mechanical morphology of shale, we integrate the confinement effect, real gas effect, effective pressure, adsorption, and end effects to develop a more accurate model of shale apparent permeability. The accuracy of this model is validated using experimental data obtained under constant effective pressure and constant confining pressure. Additionally, a comparative analysis is made against theoretical models proposed by other scholars. Finally, the impact of different transport regimes and associated model parameters on permeability is discussed. While the model developed in this study effectively couples multiple transport mechanisms based on the assumption of circular capillaries, it does not fully consider the diversity of pore geometries or the influence of organic/inorganic material differences in real shale. These aspects represent important directions for future model refinement.

2. Model

2.1. Gas thermodynamic properties

A shale matrix is characterized by a profusion of nanoscale pores, wherein gas transport is predominantly governed by external forces, colloidal forces, and the frictional force between the gas and the pore surface (Sparreboom et al., 2009). The gas thermodynamic properties within nanopores exhibit significant differences from those of bulk phase gas, which is attributed to the pronounced confinement effect. This force alters the trajectory of molecules, subsequently impacting their transport efficiency. The critical temperature and pressure of gas considering the confinement effect can be expressed as (Sun et al., 2018)

$$\frac{T_{cc}}{T_{c0}} = 1 - 1.2\left(\frac{d}{\sigma} - \frac{d_a}{\sigma}\right)^{-\frac{1}{0.88}}, \tag{1}$$

$$\frac{p_{cc}}{p_{c0}} = 1 - 1.5\left(\frac{d}{\sigma} - \frac{d_a}{\sigma}\right)^{-\frac{1}{1.6}}, \tag{2}$$

where T_{cc} is the critical temperature considering the confinement effect, K; p_{cc} is the critical pressure considering the confinement effect, Pa; T_{c0} is the critical temperature of bulk phase gas, K; p_{c0} is the critical pressure of the bulk phase gas, Pa; d is the diameter of the shale nanopores, m; d_a is the adsorbed gas thickness on the nanopore surface, m; and σ is the Lennard-Jones parameter, m.

Gas flow within shale nanopores exhibits significant real gas effects. This is primarily characterized by the gas deviation factor, viscosity, and density. Among these, the gas deviation factor can be expressed as (Yu et al., 2019)

$$Z = 0.702p_{pr}^2 e^{-2.5T_{pr}} - 5.524p_{pr}e^{-2.5T_{pr}} + 0.044T_{pr}^2 - 0.164T_{pr} + 1.15, \tag{3}$$

$$T_{pr} = \frac{T}{T_{cc}}, \tag{4}$$

$$p_{pr} = \frac{p}{p_{cc}}, \tag{5}$$

where Z is the gas deviation factor, dimensionless; T is the temperature, K; p is the pore pressure, Pa.; T_{pr} is the pseudo temperature, dimensionless; and p_{pr} is the pseudo temperature, dimensionless.

The gas density can be expressed as

$$\rho = \frac{pM}{ZRT}, \tag{6}$$

here, ρ is the gas density, kg/m^3; M is the molar mass of the gas, kg/mol; and R is the gas constant, J/(mol·K).

Under the influence of real gas effect, the momentum exchange among molecules is altered, necessitating recalculation of gas viscosity. In this context, we employ the equations proposed by Lee et al. (1966).

$$\mu_r = \left(1 \times 10^{-4}\right)\zeta \exp\left(X\rho^Y\right), \tag{7}$$

$$\zeta = \frac{(9.379 + 0.01607M)T^{1.5}}{209.2 + 19.26M + T}, \tag{8}$$

$$X = 3.448 + \frac{986.4}{T} + 0.01009M, \tag{9}$$

$$Y = 2.447 - 0.2224X, \tag{10}$$

where μ_r is the gas viscosity, Pa·s.

2.2. Bulk phase permeability model

During the flow of shale gas, various types of collisions occur. In this context, the Knudsen number (Kn) is commonly utilized to differentiate between distinct transport regimes. It plays a pivotal role in theoretical modeling, and is defined as the ratio of the average molecular free path (λ) to the pore diameter ($2r$)

$$Kn = \frac{\lambda}{2r}, \tag{11}$$

and, the average molecular free path can be expressed as (Wu et al., 2017)

$$\lambda = \frac{\mu_r}{p}\sqrt{\frac{\pi ZRT}{2M}}. \tag{12}$$

Based on the magnitude of the Kn, gas flow in nanopores is conventionally categorized into four distinct regimes, each governed by different dominant physical mechanisms:

1) Continuum flow ($Kn \leq 10^{-3}$): Intermolecular collisions dominate. The Navier-Stokes equation with no-slip boundary conditions is valid.
2) Slip flow ($10^{-3} < Kn \leq 0.1$): Intermolecular collisions still prevail, but the non-equilibrium near the wall becomes significant, requiring a slip boundary condition.
3) Transition flow ($0.1 < Kn \leq 10$): The frequencies of molecule–molecule and molecule–wall collisions are comparable. The flow is in a state between continuum and free molecular flow.
4) Knudsen (free molecular) diffusion ($Kn > 10$): Molecule–wall collisions dominate over intermolecular collisions. Gas transport is primarily driven by molecular diffusion against the walls.

Assuming that the gas flowing through the shale is nitrogen, the corresponding Knudsen number can be obtained from Eqs. (11) and (12). As can be seen in Fig. 2, within the full range of pressure, the Knudsen number decreases as the pressure increases. And observing Fig. 3, in the case of macropores, there is a coexistence of continuum flow and slip flow, while for mesopores, slip flow and transition flow coexist, and finally in micropores, transition flow and Knudsen diffusion coexist. Thus it is evident that gas flow within shale reservoirs often involves the coexistence of multiple transport regimes. It is therefore important to develop a modeling method that can effectively couple these diverse transport regimes.

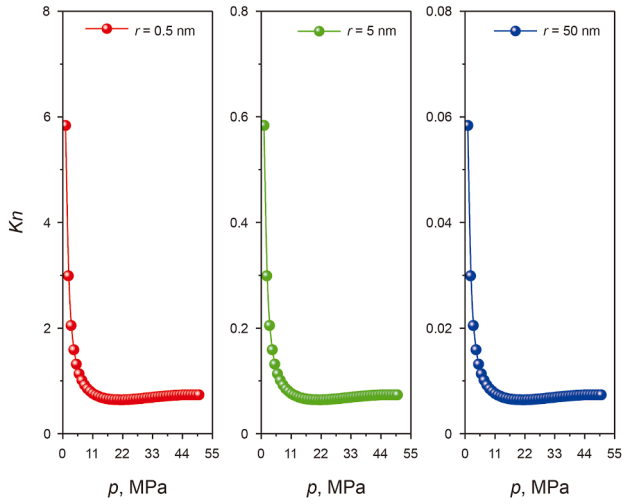

Fig. 2. Relationship between Knudsen number (Kn) and pressure (p) from model calculations (reservoir temperature is 293.15 K).

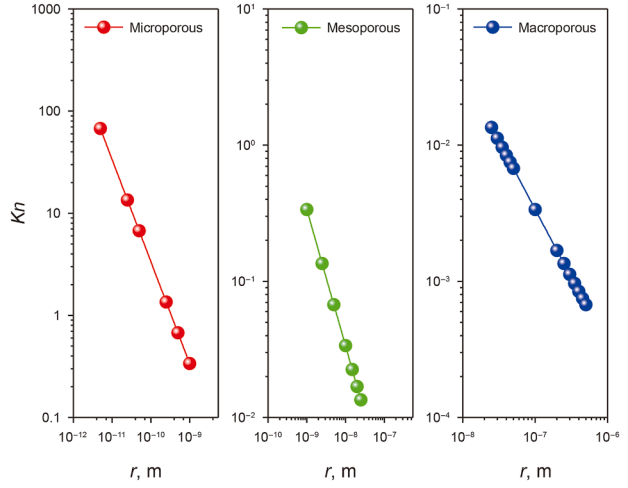

Fig. 3. Relationship between Knudsen number (Kn) and pore radius (r) from model calculations (reservoir temperature is 293.15 K; pressure is 15 MPa).

When $Kn < 10^{-3}$, the flow is considered as continuum flow, and can be described by the Hagen-Poiseuille equation, namely (Choi et al., 2001)

$$J_v = -\frac{r_0^2 pM}{8\mu ZRT}\frac{dp}{dl}, \tag{13}$$

where J_v is the mass flux of continuum flow, kg/(m^2·s); r_0 is the initial pore radius, m; and l is the distance in the direction of gas transport, m.

When $Kn > 10$, the flow is considered as Knudsen diffusion, and can be expressed as follows (Javadpour et al., 2007)

$$J_k = -\frac{2r_0 M}{3ZRT}\zeta^{D_f-2}\sqrt{\frac{8RT}{\pi M}}\frac{dp}{dl}, \tag{14}$$

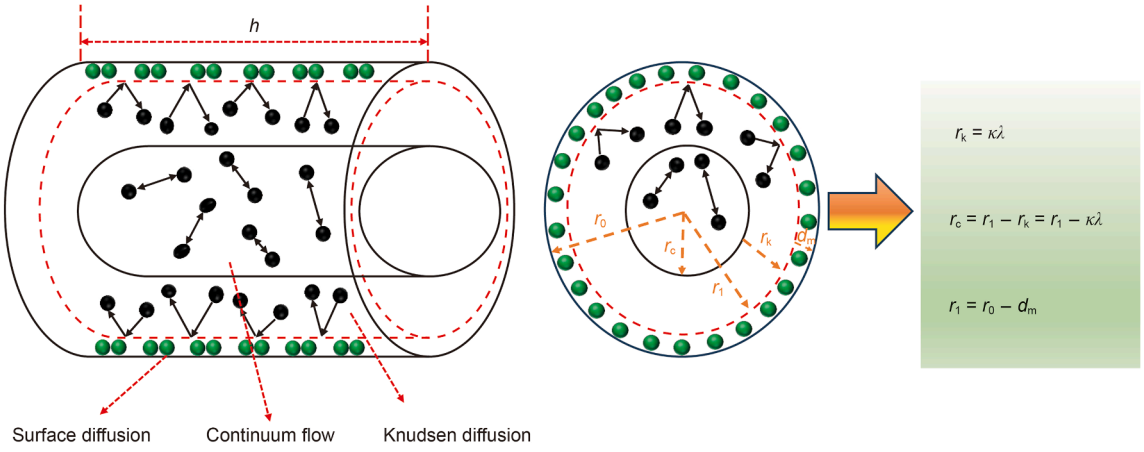

Fig. 4. Schematic diagram of shale gas transport regimes. d_m: molecular diameter.

here, J_k is the mass flux of Knudsen diffusion, kg/(m^2·s); ς is the ratio of the molecular diameter to the local pore diameter, dimensionless; and D_f is the fractal dimension of the pore surface, dimensionless.

In the process of shale gas extraction, there exists not only bulk phase gas flow driven by pressure gradients, but also surface diffusion driven by concentration gradients, as shown in Fig. 4. Among these, the flow regimes of the bulk phase gas flow are primarily characterized by continuum flow and Knudsen diffusion. Hence, both transport mechanisms must be considered in the theoretical modeling, and the core issue is to determine how to reasonably allocate the proportions of total flow flux accounted for by each flow regime. Consequently, in this study we introduce new weight coefficients, specifically: the ratios of molecule counts in the continuum flow and Knudsen diffusion to the total molecule count are used as weighting coefficients for continuum flow and Knudsen diffusion, respectively. These are then superimposed to establish a model of shale bulk phase permeability. The model assumes that: (1) the density of molecules is uniform throughout the flow region; (2) the gas type is homogeneous and the temperature remains constant throughout the flow region.

Based on the model assumptions, the molecule counts within each flow region can be calculated as follows

$$n_t = \frac{\rho h \pi r_0^2}{M}, \tag{15}$$

$$n_c = \frac{\rho h \pi r_c^2}{M}, \tag{16}$$

$$n_k = \frac{\rho h \pi (r_1^2 - r_c^2)}{M}, \tag{17}$$

where n_t is the total count of molecules, mol; n_c is the count of molecules in the continuum flow, mol; and n_k is the count of molecules in the Knudsen diffusion, mol.; h is the channel length.

Herein, the thickness of the Knudsen layer can be expressed as (Zhong et al., 1993)

$$r_k = \kappa\lambda, \tag{18}$$

the scaling factor κ in Eq. (18) characterizes the Knudsen layer thickness. According to micro-scale flow theory and inversion fitting with experimental data, the reasonable range for κ is 0.1 to 2.0. In all calculations of this study, $\kappa = 1.0$ is adopted, i.e., the Knudsen layer thickness is approximated as the gas molecular mean free path. This choice yields model results that agree well with multiple sets of experimental data.

Then, the thickness of the continuum flow region can be expressed by

$$r_c = r_1 - r_k = r_1 - \kappa\lambda, \tag{19}$$

from Eqs. (15) and (19), the respective weight coefficients for continuum flow and Knudsen diffusion can be obtained, namely

$$w_v = \frac{n_c}{n_t} = \frac{(r_1 - \kappa\lambda)^2}{r_0^2}, \tag{20}$$

$$w_k = \frac{n_k}{n_t} = \frac{r_1^2 - (r_1 - \kappa\lambda)^2}{r_1^2}, \tag{21}$$

where w_v is the weight coefficient for continuum flow, dimensionless; and w_k is the weight coefficient for Knudsen diffusion, dimensionless.

Then the mass flux of the shale bulk phase can be expressed as

$$J_b = -\frac{(r_1 - \kappa\lambda)^2}{r_1^2}\frac{{r_1}^2 pM}{8\mu ZRT}\frac{dp}{dl} - \frac{r_1^2 - (r_1 - \kappa\lambda)^2}{r_1^2}\frac{2r_1 M}{3ZRT}\varsigma^{D_f - 2}\sqrt{\frac{8RT}{\pi M}}\frac{dp}{dl}, \tag{22}$$

where J_b is the mass flux of the shale bulk phase, kg/(m^2·s).

The relationship between mass flux and permeability is

$$J = -\frac{k}{\mu}\rho\frac{dp}{dl}. \tag{23}$$

Combining Eqs. (22) and (23), the shale bulk phase permeability is then

$$k_b = \frac{(r_1 - \kappa\lambda)^2}{r_1^2}\frac{{r_1}^2 pM}{8ZRT\rho} + \frac{r_1^2 - (r_1 - \kappa\lambda)^2}{r_1^2}\frac{2r_1\mu}{3Z\rho}\varsigma^{D_f - 2}\sqrt{\frac{8M}{\pi RT}}, \tag{24}$$

where k_b is the shale bulk phase permeability, m^2.

2.3. Surface diffusion

The interior of shale is abundant with nanoscale pores, which are characterized by a large specific surface area, and where a significant volume of gas exists, predominantly in an adsorbed

state. Adsorbed gas undergoes surface diffusion under the influence of concentration gradient, which can be represented as (Wu et al., 2015b)

$$J_s = -D_s \frac{C_s}{p}\frac{dp}{dl}, \tag{25}$$

where J_s is the mass flux of surface diffusion, kg/(m^2·s); D_s is surface diffusion coefficient, m^2/s; and C_s is the adsorbed gas concentration, kg/m^3.

The adsorbed gas concentration can be expressed as (Wu et al., 2015b)

$$C_s = \frac{4\theta M}{\pi d_m^3 N_A}, \tag{26}$$

Here, d_m is the molecular diameter, m; N_A is the Avogadro constant, $N_A = 6.0221415 \times 10^{23}$ mol^{-1}; and θ is the surface coverage of the adsorbed gas, which can be expressed as

$$\theta = \frac{p}{p + p_L}, \tag{27}$$

where p_L is the Langmuir pressure, Pa.

Note that the pore surfaces are not completely covered by the gas, and therefore, the effect of the surface coverage on the surface diffusion needs to be considered. The surface diffusion coefficient can be expressed as (Chen and Yang, 1991)

$$D_s = D_s^0 \frac{(1-\theta) + \frac{\omega}{2}\theta(2-\theta) + \{H(1-\omega)\}(1-\omega)\frac{\omega}{2}\theta^2}{\left(1-\theta+\frac{\omega}{2}\theta\right)^2}, \tag{28}$$

$$H(1-\omega) = \begin{cases} 0, & \omega \geq 1 \\ 1, & 0 \leq \omega < 1 \end{cases}, \tag{29}$$

where D_s^0 is the surface diffusion coefficient when the surface coverage is "0", m^2/s; $H(1-\omega)$ is the Heaviside function, dimensionless; ω is the gas blocking coefficient, dimensionless.

After unit conversion, we can obtain the surface diffusion permeability

$$k_s = -\frac{J_s \mu V_{std}}{M dp/dl} = D_s \frac{C_s \mu V_{std}}{pM}, \tag{30}$$

where k_s is the surface diffusion permeability, m^2; V_{std} is the gas volume under standard temperature and pressure.

The shale permeability is determined through linear addition of the permeability of the bulk phase and the surface diffusion, specifically

$$k_t = k_b + k_s = \frac{(r_1 - \kappa\lambda)^2}{r_1^2}\frac{{r_1}^2 pM}{8ZRT\rho} + \frac{r_1^2 - (r_1-\kappa\lambda)^2}{r_1^2}\frac{2r_1\mu}{3Z\rho}\varsigma^{D_f-2}\sqrt{\frac{8M}{\pi RT}} + D_s\frac{C_s\mu V_{std}}{pM}, \tag{31}$$

where k_t is the shale permeability, m^2.

2.4. Shale apparent permeability

The aforementioned shale permeability model is tailored for gas migration under the assumption of constant pore size; however, in specific experimental environments, it is imperative to account for pore size variations induced by pressure alterations. Consequently, considering pore size variability is indispensable in shale permeability modeling. Hence, in this section we will incorporate pore size variations induced by pressure alterations into the aforementioned model to construct a shale apparent permeability model that is consistent with real shale gas flow behaviors.

2.4.1. Effective pressure

During the process of shale gas extraction, the pore pressure declines, leading to an increase in effective pressure, which in turn induces stress sensitivity in the matrix (Dong et al., 2010; Zhang et al., 2020). Conventional oil and gas reservoirs are characterized by an abundance of natural fractures, while shale gas reservoirs exhibit fewer natural fractures. The matrix, serving as the primary storage space for gas within the shale, directly influences the gas transport efficiency in shale formations. Therefore, the impact of effective pressure cannot be overlooked in shale gas reservoirs. Through experimental work, Dong et al. (2010) derived a relationship between permeability, porosity, and effective pressure, which can be expressed as

$$\frac{k}{k_0} = \left(\frac{p_e}{p_0}\right)^{-m}, \tag{32}$$

$$\frac{\varphi}{\varphi_0} = \left(\frac{p_e}{p_0}\right)^{-n}, \tag{33}$$

Here, k is the permeability; k_0 is the initial permeability; p_e is the effective pressure, Pa; φ is the porosity, dimensionless; φ_0 is the initial porosity, dimensionless; m is the permeability coefficient, dimensionless; and n is the porosity coefficient, dimensionless.

The permeability is correlated with the pore radius and porosity according to the following relationship (Civan, 2010)

$$r = 2\sqrt{2\tau}\sqrt{\frac{k}{\phi}}, \tag{34}$$

where τ is the tortuosity, dimensionless.

Combining Eqs. (32) and (34), the radius after considering effective pressure is

$$r_e = r_0\left(\frac{p_e}{p_0}\right)^{0.5(n-m)}, \tag{35}$$

where r_e is the pore radius after considering effective pressure, m.

2.4.2. Adsorption

The pore radius accounting for the effects of the adsorption layer and sorption-induced strain can be expressed as follows (Tian et al., 2019)

$$r_s = r_0 - \theta d_m - f\frac{t_0}{3}\Delta\varepsilon_s, \tag{36}$$

where r_s is the pore radius after considering adsorption, m; t_0 is the thickness of kerogen, m; f is the internal expansion coefficient, dimensionless, $0 < f < 1$; and $\Delta\varepsilon_s$ is the volumetric strain due to adsorption, dimensionless, which can be expressed as (Zeng et al., 2019)

$$\Delta\varepsilon_s = \varepsilon_L\frac{p/Z}{(p/Z+p_L)} - \varepsilon_L\frac{p_0/Z}{(p_0/Z+p_L)}, \tag{37}$$

where ε_L is the Langmuir strain, dimensionless; and p_0 is the initial pore pressure, Pa.

By combining Eqs. (35) and (36), we can derive the pore radius accounting for effective pressure and adsorption as follows

$$r_g = r_0 + (r_e - r_0) + (r_s - r_0) = r_0\left(\frac{p_e}{p_0}\right)^{0.5(n-m)} - \theta d_m - f\frac{t_0}{3}\Delta\varepsilon_s, \tag{38}$$

where r_g is the pore radius after considering the effects of effective pressure and adsorption, m.

2.4.3. End effects

In the previous modeling discussion, emphasis was predominantly placed on gas flow within the transport channels. This focus, however, neglects the patterns of gas flow at the inlets and outlets of the channels. For a transport channel of finite length, high viscosity shear zones are present at the inlet and outlet. This section incurs partial pressure loss due to the curvature of the streamline, a phenomenon which we refer to as "end effects", as shown in Fig. 5 (Sisan and Lichter, 2011; Weissberg, 1962). The aforementioned model does not account for the impact of end effects, and hence it is imperative to incorporate these effects when constructing an apparent permeability model. The Hagen-Poiseuille equation provides the relationship between pressure drop and flow rate excluding the end effects, and is given as follows.

$$\Delta p_\infty = \frac{8\mu L_1 Q}{\pi r^4}, \tag{39}$$

$$L_1 = \tau L_b, \tag{40}$$

where Δp_∞ is the pressure drop, Pa; Q is the flow rate, m^3/s; L_1 is the actual length of the channel, m; L_b is the length of the core, m; and τ is the tortuosity, dimensionless, which can be expressed as

$$\tau = 1 - \eta \ln(\varphi), \tag{41}$$

where η is an empirical parameter.

When gas flows through a channel, the pressure loss at the inlet and outlet of the channel is attributed to the end effects, namely (Sisan and Lichter, 2011)

$$\Delta p_{end} = \frac{3Q\mu}{r^3}, \tag{42}$$

By combining Eqs. (39) and (42), the relationship between flow rate and pressure loss after considering the influence of the end effects can be obtained, namely

$$Q_{end} = \frac{r^2}{8}\pi r^2 \frac{\Delta p}{\mu L}\frac{1}{1+\frac{3\pi}{8\psi}}, \tag{43}$$

where ψ is the ratio of channel length to radius:

$$\psi = \frac{L}{r}. \tag{44}$$

Therefore, we can obtain the pore radius after considering the influence of end effects as

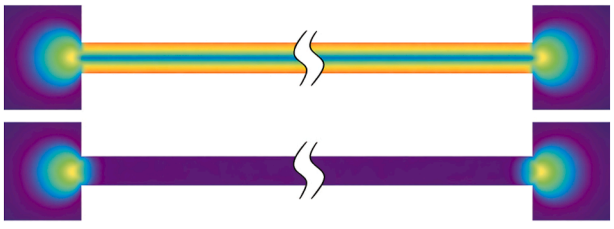

Fig. 5. Energy dissipation (high (light purple), low (dark purple)) (Sisan and Lichter, 2011).

$$r_{end} = r_g\sqrt{1+\frac{3\pi}{8\psi}}. \tag{45}$$

From Eq. (45), it is evident that neglecting the end effects results in an underestimation of the size of the channel. Therefore, by combining Eqs. (38) and (45), we can determine the pore radius accounting for effective pressure, adsorption, and end effects as

$$r_{eff} = \left(r_0\left(\frac{p_e}{p_0}\right)^{0.5(n-m)} - \theta d_m - f\frac{t_0}{3}\Delta\varepsilon_s\right)\sqrt{1+\frac{3\pi}{8\psi}}. \tag{46}$$

In the context of shale gas reservoirs, assuming that they are constituted by cylindrical tubes, the model can be represented as (Civan, 2019)

$$\varphi = n\pi r^2\tau, \tag{47}$$

$$k = \frac{r^2}{8}\frac{\varphi}{\tau^2}. \tag{48}$$

From Eqs. (47) and (48), we can derive the relationship between permeability and pore radius as:

$$\frac{k}{k_0} = \left(\frac{r}{r_0}\right)^4, \tag{49}$$

and upon rearranging Eqs. (31), (46) and (49), we obtain

$$k_{app} = \left[\frac{(r_1-\kappa\lambda)^2 r_1^2 pM}{r_1^2 \quad 8ZRT\rho} + \frac{r_1^2-(r_1-\kappa\lambda)^2}{r_1^2}\frac{2r_1\mu}{3Z\rho}\varsigma^{D_f-2}\sqrt{\frac{8M}{\pi RT}} + D_s\frac{C_s\mu V_{std}}{pM}\right] \left[\frac{\left(r_0\left(\frac{p_e}{p_0}\right)^{0.5(n-m)} - \theta d_m - f\frac{t_0}{3}\Delta\varepsilon_s\right)\sqrt{1+\frac{3\pi}{8\psi}}}{r_0}\right]^4, \tag{50}$$

where k_{app} is the apparent permeability, m^2.

3. Model validation

Traditional permeability models are predominantly constructed based on empirical relationships, and often fall short in accurately characterizing gas flow behaviors. During extraction of shale gas, the apparent permeability is significantly influenced by variations in factors such as transport regimes, confinement effects, real gas effects, end effects, and adsorption. Consequently, we establish an apparent permeability model by coupling the aforementioned transport mechanisms and microscale effects, building upon a capillary model foundation. In this section, the accuracy of the shale apparent permeability model will be validated under various experimental boundary conditions, including constant effective pressure and constant confining pressure.

3.1. Constant effective pressure

First, we utilized experimental data under constant effective pressure to validate the proposed model. Experimental data under constant effective pressure were collected from the work of Li et al. (2020). The experimental core samples were sourced from the Barnett, Eagle Ford, and Marcellus shale reservoirs in the United States. A pulse decay permeameter and N2 were used in the experimental procedure. The experiments were conducted at effective pressurees of 3.4 MPa and 6.8 MPa, and a temperature of

Table 1
Basic input parameters.

Parameters	Values	References	Values	References	Values	References
Shale samples	Barnett	Li et al. (2020)	Eagle Ford	Li et al. (2020)	Marcellus	Li et al. (2020)
Gas type	N_2	Li et al. (2020)	N_2	Li et al. (2020)	N_2	Li et al. (2020)
Molecular weight M	0.028 kg/mol	-	0.028 kg/mol	-	0.028 kg/mol	-
Temperature T	293.15 K	Li et al. (2020)	293.15 K	Li et al. (2020)	293.15 K	Li et al. (2020)
Internal expansion coefficient f	0.0832 (3.4 MPa) 0.0476 (6.8 MPa)	Data fitting	0.0417 (3.4 MPa) 0.0013 (6.8 MPa)	Data fitting	0.0254 (3.4 MPa) 0.0122 (6.8 MPa)	Data fitting
Critical pressure p_c	3.39×10^6 Pa	Gao et al. (2021a)	3.39×10^6 Pa	Gao et al. (2021a)	3.39×10^6 Pa	Gao et al. (2021a)
Critical temperature T_c	126.2 K	Gao et al. (2021a)	126.2 K	Gao et al. (2021a)	126.2 K	Gao et al. (2021a)
Langmuir pressure p_L	2×10^6 Pa	Gao et al. (2021b)	2×10^6 Pa	Gao et al. (2021b)	2×10^6 Pa	Hatami et al. (2020)
Langmuir strain ε_L	0.05	Gao et al. (2021c)	0.05	Gao et al. (2021c)	0.02295	Wang et al. (2018b)
Thickness of kerogen t_0	1×10^{-6} m	Gao et al. (2021c)	1×10^{-6} m	Gao et al. (2021c)	1×10^{-6} m	Gao et al. (2021c)
Surface diffusion coefficient at $\theta = 0$ D_s^0	1×10^{-8}~1×10^{-4} m^2/s	Shen et al. (2018)	1×10^{-8}~1×10^{-4} m^2/s	Shen et al. (2018)	1×10^{-8}~1×10^{-4} m^2/s	Shen et al. (2018)
Blocking coefficient of gas molecule ω	0.5	Wu et al. (2016)	0.5	Wu et al. (2016)	0.5	Wu et al. (2016)
Molecular diameter d_m	0.364 nm	-	0.364 nm	-	0.364 nm	-
Pore radius r	5×10^{-9} m	Adesida et al. (2011); Chalmers et al. (2012); Gao et al. (2021d); Shen et al. (2018)	1×10^{-8} m	Gao et al. (2021d); Rylander et al. (2013); Shen et al. (2018)	4×10^{-9} m	Chalmers et al. (2012); Gu et al. (2015)
Porosity φ	0.04	Gao et al. (2021d)	0.04	Gao et al. (2021d)	0.04	Gao et al. (2021d)
Coefficient for tortuosity calculation η	0.77	Kazemi and Takbiri-Borujeni (2015)	0.77	Kazemi and Takbiri-Borujeni (2015)	0.77	Kazemi and Takbiri-Borujeni (2015)
Permeability coefficient m	0.3961 (3.4 MPa) 0.4372 (6.8 MPa)	Data fitting	1.5060 (3.4 MPa) 1.1627 (6.8 MPa)	Data fitting	1.5108 (3.4 MPa) 1.0815 (6.8 MPa)	Data fitting
Porosity coefficient n	0.0299 (3.4 MPa) 0.0298 (6.8 MPa)	Data fitting	0.0248 (3.4 MPa) 0.0258 (6.8 MPa)	Data fitting	0.0251 (3.4 MPa) 0.0242 (6.8 MPa)	Data fitting

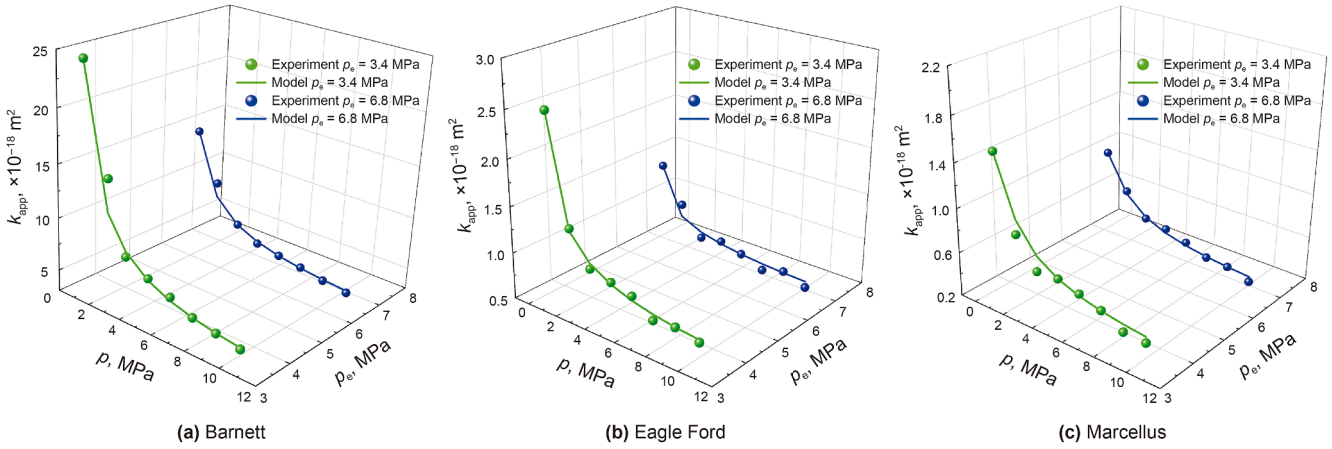

Fig. 6. Comparison between experimental data and model results (p_e: effective pressure; p: pore pressure; k_{app}: apparent permeability).

20 °C. The sample was 5.08 cm in length and 2.54 cm in diameter. Utilizing the model parameters from Table 1 and plugging into Eq. (50), the model results were obtained and subsequently compared with the experimental data, as illustrated in Fig. 6.

As depicted in Fig. 6, the apparent permeability of the three shale reservoirs exhibits the same trend: namely, as the pore pressure increases, the apparent permeability declines gradually. This observation underscores the intrinsic correlation between enhanced pore pressure and reduced flow capacity. Upon investigation, it is found that under low pressure, the microscale effects are significant. Moreover, the enhanced interactions between molecules and the pore surface increase the gas transport efficiency. As pore pressure increases, free gas gradually becomes adsorbed gas, which is accompanied by an enhanced sorption-induced strain, and this leads to a narrowing of the transport channels. Furthermore, it can be observed from Eq. (12) that an increase in pore pressure leads to a reduction in the average molecular free path, attenuating the interaction strength between the gas molecules and pore walls. Consequently, there is a discernible decreasing trend in apparent permeability.

3.2. Constant confining pressure

To further demonstrate the universality of the model, experimental data obtained under constant confining pressure are next used to validate its accuracy. This experimental data were gathered from the work of Ghanizadeh et al. (2014). The core samples were extracted from the HAD1 and HAD2 wells located in the Posidonia

region of Germany. The sample from the HAD1 well measured 26.70 mm in length and 27.20 mm in diameter, while the sample from the HAD2 well had a length of 8.47 mm and a diameter of 28.05 mm. The experiment was conducted using the steady-state method, at a temperature of 45 °C, with methane (CH_4) as the test gas. The model parameters from Table 2 are substituted into Eq. (50) to obtain the model results, which are then compared with the experimental data, as illustrated in Fig. 7.

As illustrated in Fig. 7, there is strong overlap between the experimental data and the model-predicted values, exhibiting a similar variation trend as in Fig. 6. This high level of consistency further corroborates the accuracy of the model.

3.3. Model comparison

To further validate the superiority of the new model, the experimental data and parameters from Table 1 are substituted into Eqs. (51) and (52), respectively, yielding curves of apparent permeability variation with pore pressure. These are then compared with the curve obtained from the new model, as illustrated in Fig. 8. Eq. (51) is referred to as the "Lu" model (Lu et al., 2016) and Eq. (52) is termed the "S&D" model (Shi and Durucan, 2004). The parameters for the three models are listed in Table 3.

$$k = k_0 \exp\left\{ -3C_f \left[-(p-p_0) + f\frac{E}{3(1-2\nu)}\frac{\varepsilon_L p_L (p-p_0)}{(p+p_L)(p_0+p_L)} \right] \right\}, \tag{51}$$

$$k = k_0 \exp\left\{ -3C_f \left[-\frac{\nu}{1-\nu}(p-p_0) + \frac{E}{3(1-\nu)}\varepsilon_L \left(\frac{p}{p+p_L} - \frac{p_0}{p_0+p_L} \right) \right] \right\}, \tag{52}$$

where k_0 is the initial permeability, m^2; E is the Young's modulus, Pa; C_f is the cleat compressibility, Pa^{-1}; and υ is the Poisson's ratio, dimensionless.

As can be observed from Fig. 8, compared with the "Lu" and "S&D" models, all three models can capture the relationship between apparent permeability and pore pressure; however, the new model exhibits a higher degree of fit. The reasons for this are multifaceted: (1) The "Lu" model is established under constant confining pressure, whereas the "S&D" model is constructed under uniaxial strain conditions, and the experimental condition is that of constant effective pressure. (2) Both the "Lu" and "S&D" models are established under fractured conditions. (3) Both the "Lu" and the "S&D" models have not accounted for end effects, Knudsen diffusion, and surface diffusion. From Section 2, it is evident that these three phenomena influence the shale apparent permeability; because the new model considers these transport mechanisms, the result is higher model fidelity.

Furthermore, beyond merely incorporating more mechanisms, the proposed weighting method itself offers a physically more robust foundation for coupling flow regimes. Traditional superposition models often rely on empirical or semi-empirical coefficients to combine continuum flow and Knudsen diffusion, which lack a clear mechanistic justification. In contrast, our method weights these regimes based on the proportion of gas molecules that actually reside in each corresponding flow region (i.e., the continuum core and the Knudsen layer). This approach directly reflects the physical distribution of molecules within the nanopore, as depicted in Fig. 4, and provides a seamless transition between flow regimes governed by molecular statistics rather than fitted parameters. This inherent physical rationale is a key reason for the model's improved predictive accuracy across a wide range of pore pressures and radii.

4. Discussion

Shale exhibits a complex pore structure, and its permeability is influenced by various factors. However, the controlling factors and mechanisms related to shale permeability remain poorly understood. In this section, we discuss the evolution of apparent permeability under various controlling factors. Table 4 presents

Table 2
Basic input parameters.

Parameters	Values	References
Shale samples	Posidonia	Ghanizadeh et al. (2014)
Gas type	CH_4	Ghanizadeh et al. (2014)
Molecular weight M	0.016 kg/mol	-
Temperature T	318.15 K	Ghanizadeh et al. (2014)
Internal expansion coefficient f	0.0105 (24.8 MPa=HAD1) 0.0009 (31 MPa=HAD1) 0.0200 (7.5 MPa=HAD2) 0.0100 (23 MPa=HAD2)	Data fitting
Critical pressure p_c	4.59×10^{-6} Pa	Gao et al. (2021a)
Critical temperature T_c	190.4 K	Gao et al. (2021a)
Langmuir pressure p_L	2×10^{-6} Pa	Gao et al. (2021b)
Langmuir strain ε_L	0.07	Gao et al. (2021b)
Thickness of kerogen t_0	1×10^{-6} m	Gao et al. (2021c)
Surface diffusion coefficient at $\theta = 0$ D_s^0	1×10^{-8}~1×10^{-4} m^2/s	Shen et al. (2018)
Blocking coefficient of gas molecule ω	0.5	Wu et al. (2016)
Molecular diameter d_m	0.38 nm	-
Pore radius r	3×10^{-8} m	Gao et al. (2021d); Grathoff et al. (2016)
Porosity φ	0.063	Gao et al. (2021d)
Coefficient for tortuosity calculation η	0.7	Kazemi and Takbiri-Borujeni (2015)
Permeability coefficient m	0.3808 (24.8 MPa=HAD1) 0.3947 (31 MPa=HAD1) 0.5686 (7.5 MPa=HAD2) 0.3983 (23 MPa=HAD2)	Data fitting
Porosity coefficient n	0.0207 (24.8 MPa=HAD1) 0.0269 (31 MPa=HAD1) 0.0282 (7.5 MPa=HAD2) 0.0292 (23 MPa=HAD2)	Data fitting

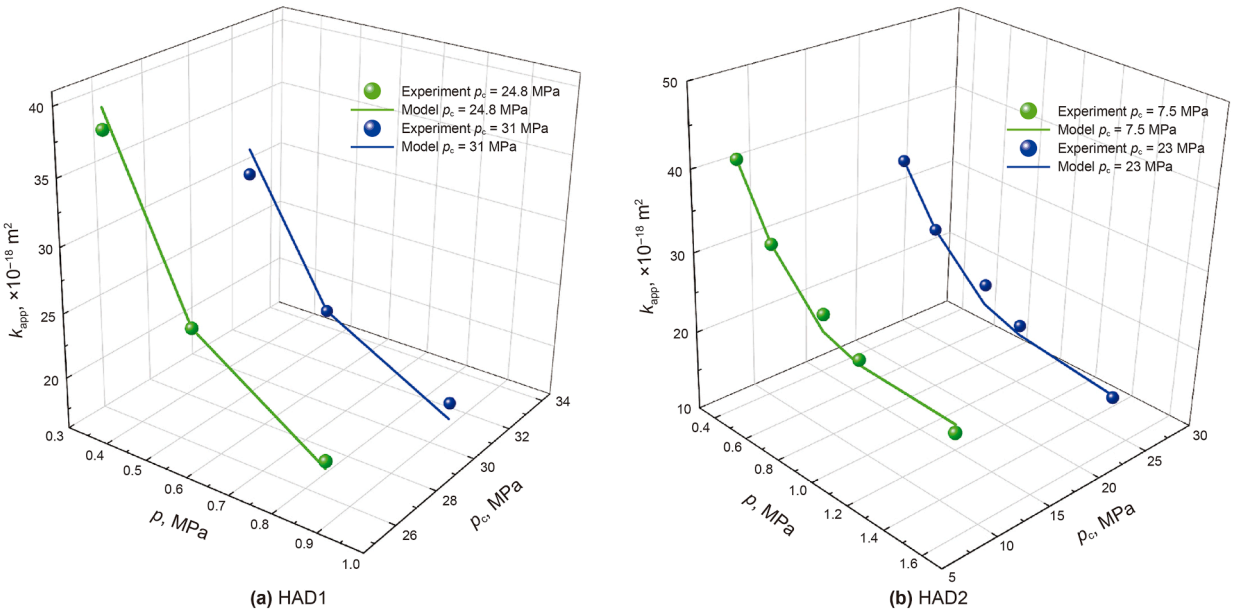

Fig. 7. Comparison between experimental data and model results. p_c: confining pressure; p: pore pressure; k_{app}: apparent permeability. Data source: Ghanizadeh et al. (2014).

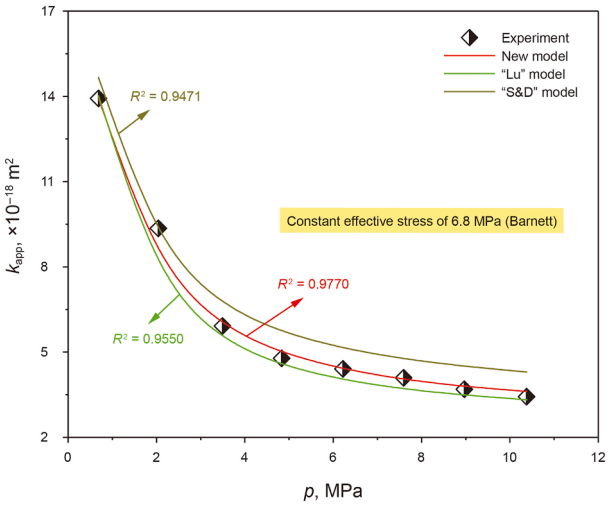

Fig. 8. Comparison of the three models (p: pore pressure; k_{app}: apparent permeability) (Barnett).

Table 3
Model parameters (three models).

Parameters	New model	"Lu" model	"S&D" model
Initial permeability k_0, × 10^{-18} m^2	-	26.7747	25.0119
Cleat compressibility C_f, MPa^{-1}	-	0.0014	0.0010
Porosity coefficient n	0.0298	-	-
Permeability coefficient m	0.4372	-	-
Internal expansion coefficient f	0.0476	0.5237	-
Coefficient of determination R^2	0.9770	0.9550	0.9471

the relevant model parameters used as an example in this discussion.

4.1. Analysis of the impact of different transport regimes

Fig. 9 depicts the relationship between the apparent permeability deviation and pore pressure for pore radii of 5 nm, 10 nm, 25 nm, and 50 nm, disregarding different mechanisms of action. In this context, a positive value indicates that neglecting this mechanism would result in an overestimation of the apparent permeability, whereas a negative value would result in an underestimation.

As illustrated in Fig. 9, ignoring surface diffusion and end effects results in an underestimation of the apparent permeability. In contrast, ignoring effective pressure can lead to an overestimation. In the initial stage of pressure loading, the real gas effect tends to overestimate the actual value; conversely, in the later stages the tendency is to underestimate. The real gas effect plays a significant role in the transport process of shale gas. Specifically, under low pressure conditions, the intermolecular forces are attractive, leading to a reduced average molecular free path. Consequently, the interaction strength between the molecules and the pore surface increases, resulting in a decreased transport capacity. Under high pressure conditions, the intermolecular forces are repulsive, leading to an increase in the average molecular free

Table 4
Relevant parameters.

Parameters	Values
Gas type	N_2
Molecular weight M	0.028 kg/mol
Temperature T	293.15 K
Internal expansion coefficient f	0.1, 0.3, 0.5, 0.7, 0.9
Critical pressure p_c	3.39 × 10^6 Pa
Critical temperature T_c	126.2 K
Langmuir pressure p_L	2 × 10^6 Pa
Langmuir strain ε_L	0.05
Thickness of kerogen t_0	1 × 10^{-6} m
Surface diffusion coefficient at $\theta = 0$ D_s^0	1 × 10^{-8} m^2/s
Blocking coefficient of gas molecule ω	0.5
Molecular diameter d_m	0.364 nm
Pore radius r	5 × 10^{-9}–5 × 10^{-7} m
Porosity φ	0.04
Coefficient for tortuosity calculation η	0.77
Permeability coefficient m	0.01, 0.03, 0.05, 0.07, 0.09
Porosity coefficient n	0.006, 0.008, 0.010, 0.012, 0.014
Ratio of channel length to radius ψ	1.5, 2.5, 3.5, 4.5, 5.5, 6.5
Volumetric strain $\Delta\varepsilon$	0.005, 0.02, 0.04, 0.06

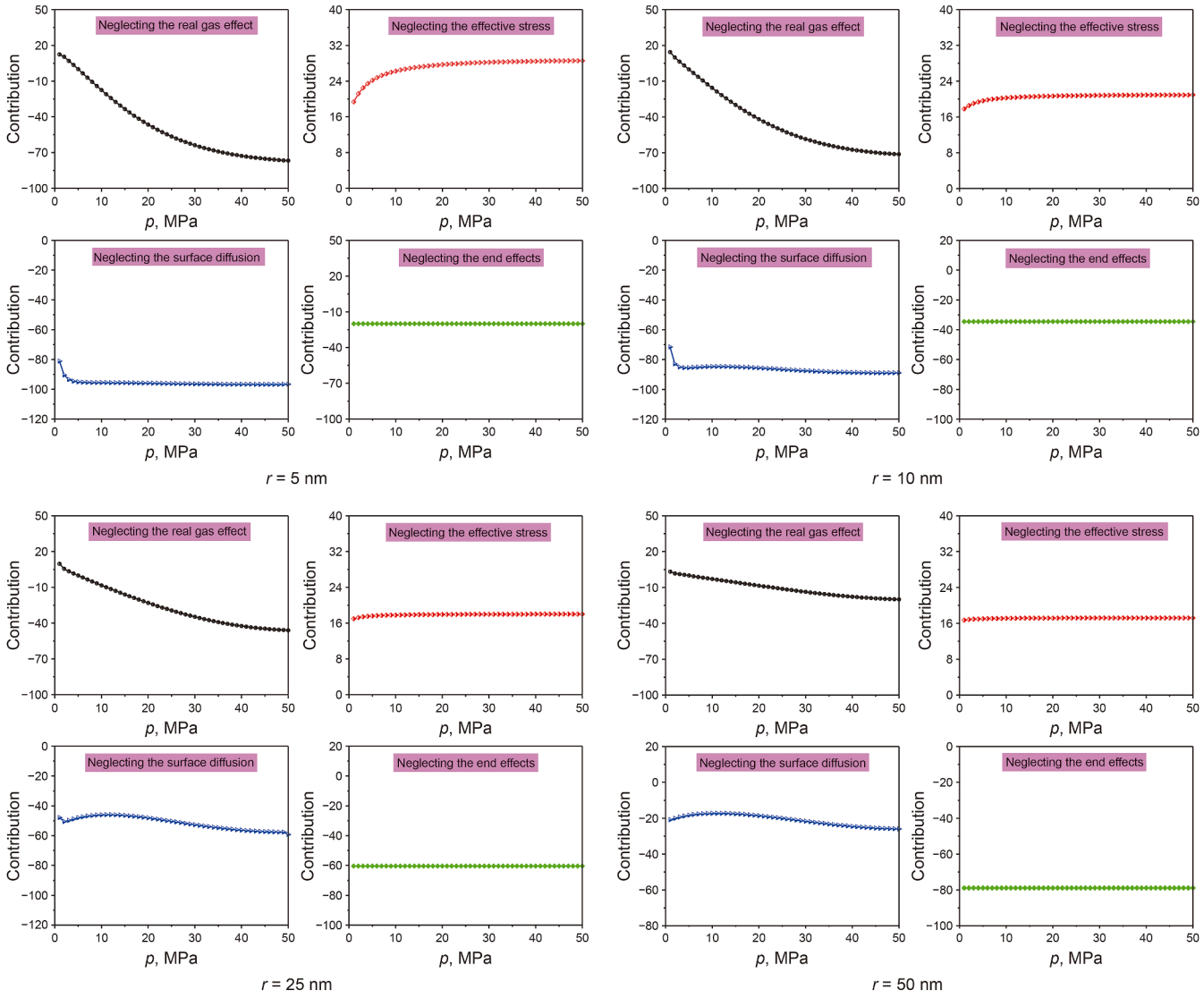

Fig. 9. Effect of different action mechanisms on the shale apparent permeability. *r*: pore radius; *p*: pore pressure.

path. The interaction strength between the molecules and the pore surface thus decreases, enhancing their transport capability. However, for shale reservoirs, there is significant pore pressure. Thus the real gas effect enhances the transport capacity of shale gas. This influence increases with rising pressure and diminishing pore radius. In terms of effective pressure, the deviation increases with rising pore pressure; furthermore, the smaller the pore radius, the greater the deviation.

The underlying reasons for this are multifold: under identical conditions, the magnitude of variation in smaller pores is proportionally larger than that in larger pores, thereby exerting a greater influence on the smaller pores. For surface diffusion, its impact is more significant when the pore radius is small, whereas its influence diminishes as the pore diameter increases. For the end effects, it is evident from Eq. (45) that these phenomena are solely related to the channel length and radius and are independent of pressure. As the pore radius increases, the impact of the end effects becomes progressively stronger. In summary, at a pore radius of 5 nm, the surface diffusion and real gas effect are most pronounced, followed by effective pressure, and then end effects are the least significant. At a pore radius of 10 nm, the surface diffusion and real gas effect are most pronounced, followed by end effects, and then effective pressure is the least significant. At a pore radius greater than or equal to 25 nm, the end effects have the most influence, while surface diffusion and effective pressure have comparable impacts, and the real gas effect is the least pronounced.

The ability to quantify the contribution of each mechanism stems directly from the molecule-count-based weighting framework. By distinguishing molecules in the Knudsen layer from those in the continuum core, the model naturally partitions the total flux into components governed by wall-collision-dominated (Knudsen) and intermolecular-collision-dominated (continuum) transport. This partitioning not only allows for the linear superposition of surface diffusion but also provides a transparent and physically interpretable basis for sensitivity analyses, such as those shown in Fig. 9. Consequently, the model not only predicts apparent permeability more accurately but also offers a diagnostic tool to identify which transport mechanism dominates under given reservoir conditions (e.g., pore size, and pressure).

4.2. End effects

As stated in Section 2.4.3, the end effects have a direct impact on the model's predicted values and should not be disregarded. Therefore, in this section we will examine the impact of end effects on the apparent permeability. Specifically, we investigate the relationship between apparent permeability and pore pressure for various ψ values to better understand gas flow within shale. As depicted in Fig. 10, the apparent permeability gradually decreases as ψ values increase. This is because the end effects are responsible for the pressure loss. Ignoring the influence of end effects means that the pressure loss at the inlets and outlets of channels are included in the internal pressure loss of the channels. Therefore, calculating the pore radius without considering end effects will underestimate the pore size. The larger the ψ value, the smaller the actual pore size after considering the end effects, resulting in narrower transport channel and a decrease in apparent permeability.

(1) End effects essentially represent additional pressure drops at the inlet and outlet, which can be significant both in laboratory core-scale measurements (finite length) and in near-wellbore flow through proppant packs. (2) Traditional models neglecting this effect mistakenly attribute this pressure drop to the internal flow resistance of the core, leading to a systematic underestimation of apparent permeability (as shown in Fig. 9, which can be substantial for larger pores). (3) By being the first to incorporate end effects, our model not only improves fitting accuracy (as shown in Fig. 8) but, more importantly, provides a theoretical tool for correcting laboratory permeability measurements and more accurately predicting gas flow efficiency in the near-wellbore region. This directly addresses practical challenges in the efficient development of shale gas resources.

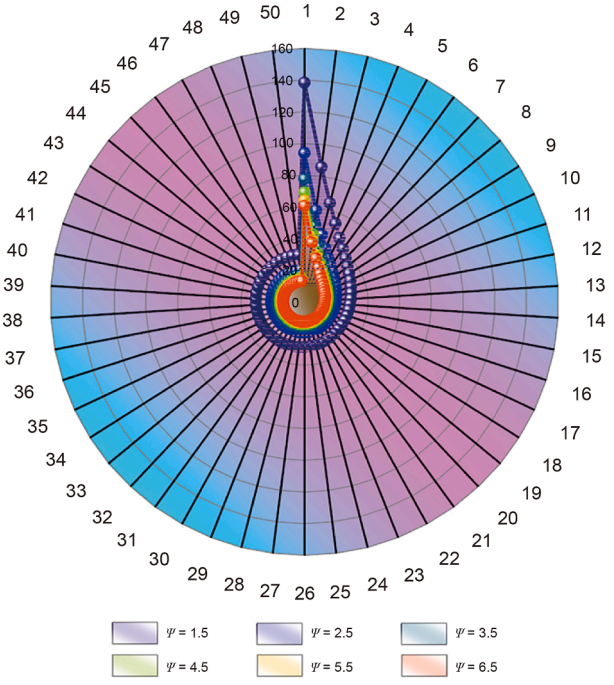

Fig. 10. Relationship between apparent permeability and pore pressure under different values of ψ. ψ, ratio of channel length to radius.

4.3. Volumetric strain

Adsorption plays a significant role in the proposed shale apparent permeability model. Hence in this section, we select four different sets of parameters for volumetric strain to investigate their effects on shale apparent permeability. As can be seen from Fig. 11, the apparent permeability decreases with increasing volumetric strain. (1) This decrease is caused by the larger volumetric strain, indicating a significant transformation of free gas into adsorbed gas, which results in decreased transport efficiency. (2) The larger volumetric strain makes a bigger contribution to pore shrinkage, further contributing to the decrease in apparent permeability.

4.4. Discussion of parameters

In the new model, three fitting parameters are introduced: a permeability coefficient, a porosity coefficient, and an internal swelling coefficient. This section will analyze the impact of these three parameters on shale gas transport behavior.

From Eqs. (32) and (33), a power-law relationship is utilized to depict the relationship between the permeability coefficient, porosity coefficient, and effective pressure in the model. Therefore we can explore the influence of different values of these coefficients on apparent permeability, with results presented in Figs. 12 and 13. As shown in Fig. 12, the apparent permeability decreases with an increasing permeability coefficient under the same pore pressure. The permeability coefficient thus indicates the sensitivity of the apparent permeability to changes in effective pressure. A higher permeability coefficient implies greater sensitivity of the pores to effective pressure, resulting in reduced apparent permeability. As depicted in Fig. 13, for the same pore pressure, as the porosity coefficient increases, the apparent permeability also increases; however the magnitude of the increase is minimal. Based on Eq. (34), there is an inverse relationship between pore radius and porosity. A smaller porosity corresponds to a larger pore radius, leading to increased transport efficiency and, thereby, a higher apparent permeability.

The internal swelling coefficient (f) is a crucial factor for quantifying the impact of volumetric strain on the apparent permeability, $0 < f < 1$. Fig. 14 illustrates the relationship between

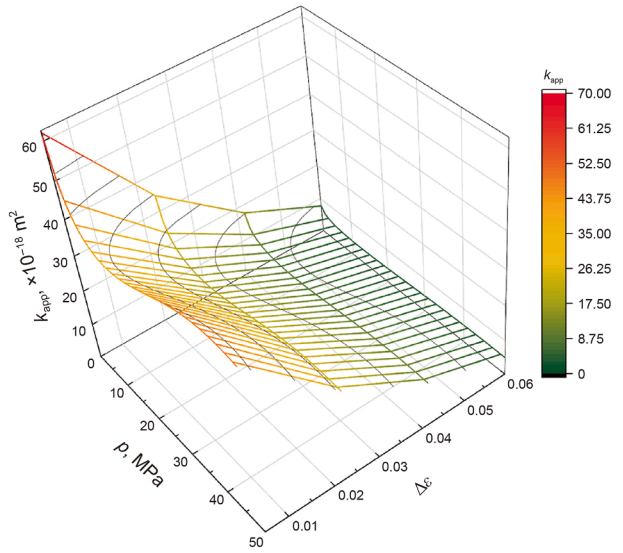

Fig. 11. Relationship between apparent permeability (k_{app}) and pore pressure (p) under different volumetric strain ($\Delta\varepsilon$).

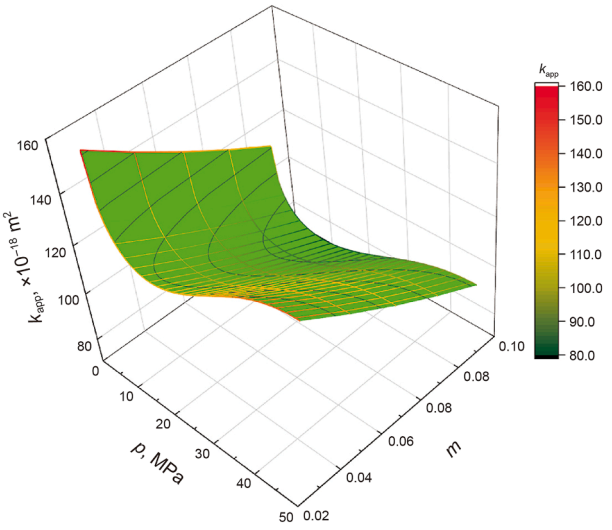

Fig. 12. Effect of permeability coefficient (m) on apparent permeability (k_{app}).

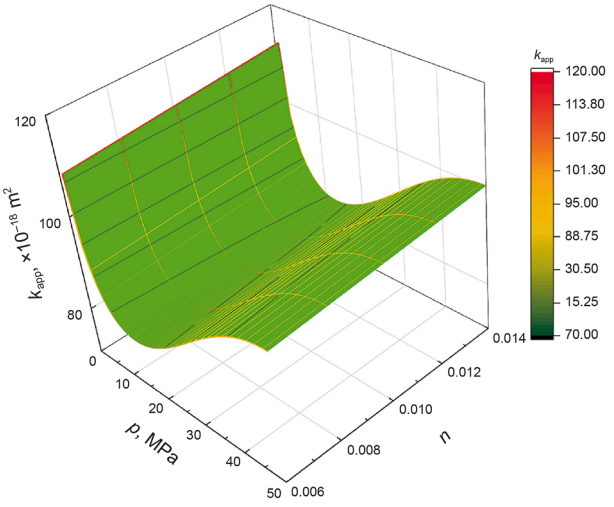

Fig. 13. Effect of porosity coefficient (n) on apparent permeability (k_{app}).

apparent permeability and pore pressure under different internal swelling coefficients. As one can observe, when the pore pressure is held constant, the apparent permeability decreases as the internal swelling coefficient increases. The reasons for this are as follows: when the internal swelling coefficient is greater, the contribution of volume strain to pore contraction is larger, leading to a decrease in transport efficiency; secondly, the smaller the pore size, the smaller the intrinsic permeability, further resulting in a decrease in apparent permeability.

4.5. Model foresight

Shale possesses a complex pore structure comprised of pores of various shapes, including circular, square, equilateral triangular, and others. In this study, we assume that the pore morphology is of a circular shape, which introduces certain limitations. To better describe the flow behaviors of shale gas, here we focus on circular, square, and equilateral triangular geometries (Fig. 15), aiming to develop a more comprehensive

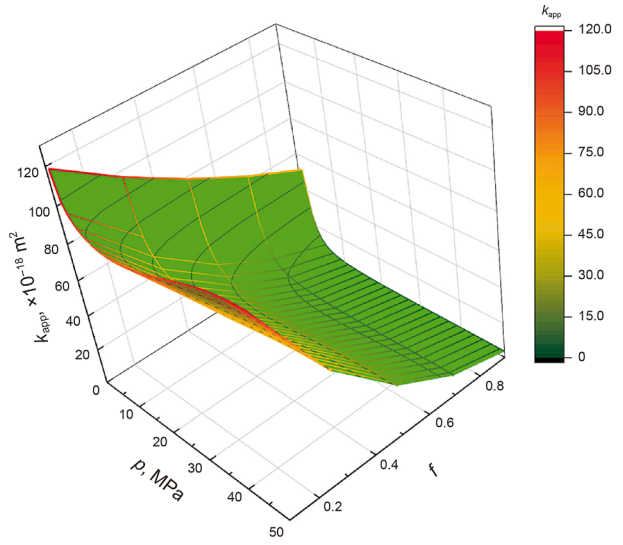

Fig. 14. Effect of internal swelling coefficient (f) on apparent permeability (k_{app}).

apparent permeability model for shale. Hence, the apparent permeability of shale can be expressed as

$$k_i = \left(w_{v,i}k_{v,i} + w_{k,i}k_{k,i}\right) + k_{s,i}, \tag{53}$$

here, the subscript i = 1, 2, 3 represents circular, square, and equilateral triangular pores, respectively. $k_{v,i}$ and $k_{k,i}$ are the permeability contributions from continuum flow and Knudsen diffusion in pores of the corresponding shape. Their weighting coefficients, $w_{v,i}$ and $w_{k,i}$, are calculated following the same logic as the main model (Section 2.2), determined by the thickness of the Knudsen layer. $k_{s,i}$ is the surface diffusion permeability for the corresponding pore shape. The key lies in defining the mathematical expressions for $k_{v,i}$ and $k_{k,i}$ under different shapes.

(a) Circular pores

For a straight circular capillary with radius r, its permeability model is the main model of this study. The continuum flow part is given by the Hagen-Poiseuille equation, and the Knudsen diffusion part adopts the form proposed by (Javadpour et al., 2021). The specific expressions have been derived in detail in Sections 2.1 to 2.3 (Eqs. (13), (14), (24) and (30)) and can be directly referenced. That is

$$k_1 = k_t, \tag{54}$$

where is defined by Eq. (31).

(b) Square pores

For a pore with a square cross-section and hydraulic diameter D_h, its continuum flow (slip flow) permeability $k_{v,2}$ can be expressed as (Morini, 2004)

$$k_{v,2} = \frac{d_h^2}{32}(1 + \alpha Kn), \tag{55}$$

where α is the slip coefficient, and d_h is the hydraulic diameter (for a square with side length y, $d_h = y$. The Knudsen diffusion permeability $k_{k,2}$ can be analogized to the expression for circular

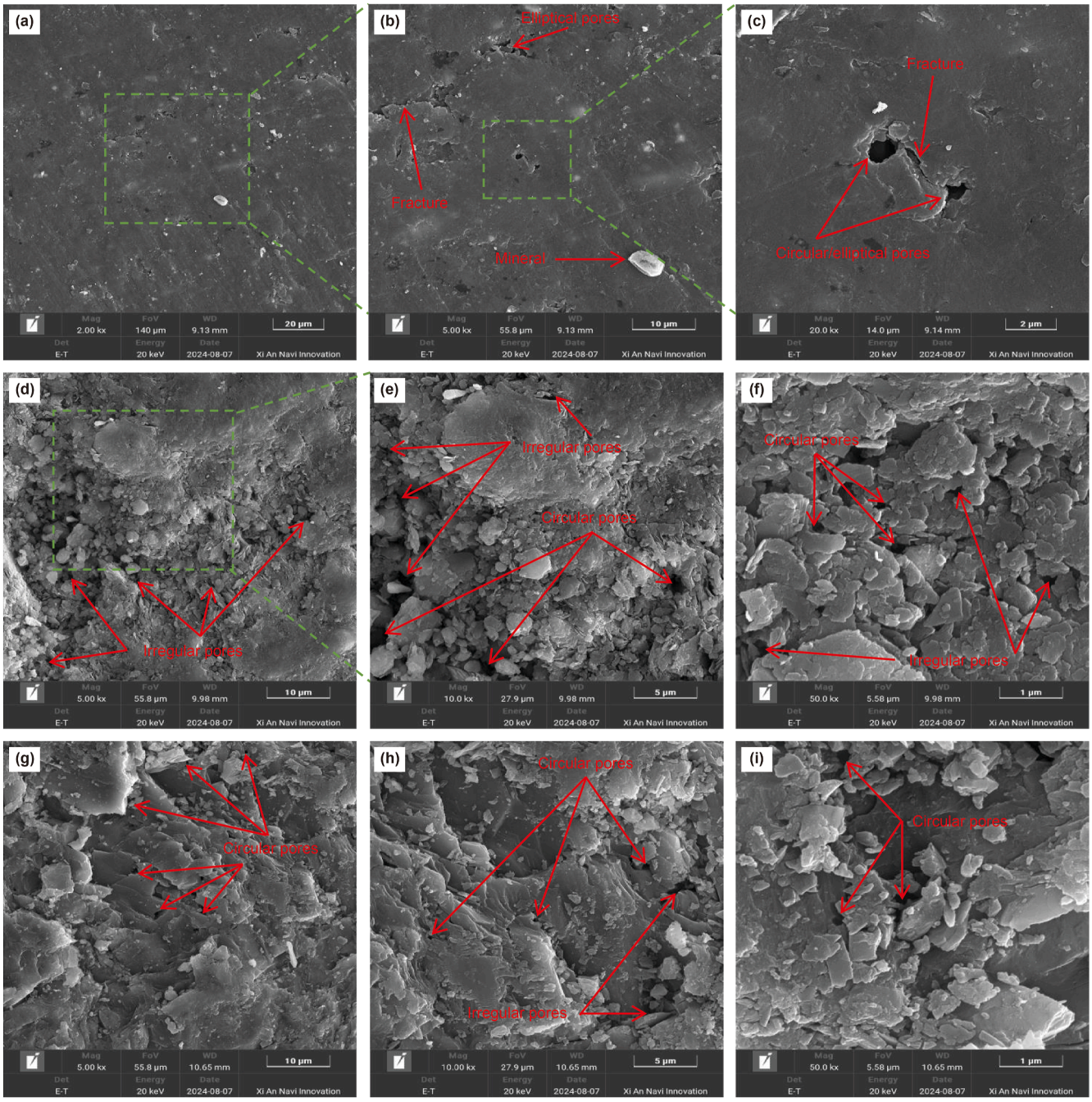

Fig. 15. Surface pore and fracture morphologies relating to effective helium source rocks. The first row (**(a)–(c)**), second row (**(d)–(f)**), and third row (**(g)–(i)**) displayed the scanning electron microscopy results for coal, shale, and granite at different magnifications, respectively (Song et al., 2025).

pores but requires consideration of a shape factor, often expressed as (Graur et al., 2009)

$$k_{k,2} = \phi_2 \cdot \frac{d_h}{3}\sqrt{\frac{8ZRT}{\pi M}}\,\frac{\mu}{p}, \tag{56}$$

here, ϕ_2 is the shape correction factor for square pores (typically close to 1).

(c) Equilateral triangular pores

For an equilateral triangular pore with side length **b**, its continuum flow permeability $k_{v,3}$ is (Duan and Muzychka, 2007)

$$k_{v,3} = \frac{b^2}{80}(1 + \alpha' Kn), \tag{57}$$

where α' is the corresponding slip coefficient. Its Knudsen diffusion permeability $k_{k,3}$ can be expressed in a form similar to that for square pores (Graur et al., 2009)

$$k_{k,3} = \phi_3 \frac{d_{h,3}}{3}\sqrt{\frac{8ZRT}{\pi M}}\,\frac{\mu}{p}, \tag{58}$$

where $d_{h,3}$ is the hydraulic diameter of the equilateral triangle ($d_{h,3} = b/\sqrt{3}$), and ϕ_3 is the corresponding shape correction factor.

By substituting the above $k_{v,i}$ and $k_{k,i}$ into the weighting model and combining them with the surface diffusion term $k_{s,i}$ (whose form is independent of shape and depends primarily on specific surface area and adsorption parameters; refer to Eq. (30)), k_2 and k_3 can be calculated. Finally, by performing a volume-weighted average of the permeabilities for different shapes using Eq. (53), a more accurate prediction model for shale apparent permeability that better reflects the real complex pore structure (mixed shapes) can be obtained.

Therefore, future model improvements should focus on: (1) Developing a permeability model that couples multiple pore geometries, such as incorporating weighted contributions from typical pore shapes like circular, slit-shaped, and triangular pores to better reflect the influence of pore morphology; (2) Introducing a dual-system model for organic and inorganic pores, separately describing gas transport mechanisms in organic and inorganic pores while considering their differences in adsorption, diffusion, and stress-dependent deformation; (3) Integrating digital rock or pore-network models to simulate flow in more realistic pore structures, thereby validating and extending the applicability of the proposed model.

5. Conclusions

Novel models describing gas flow in shale were proposed, based on a capillary model and using the proportions of molecule counts in different regions relative to the total molecule counts as weighting coefficients. We coupled continuum flow with Knudsen diffusion to establish a shale bulk phase permeability model. Building upon this, an apparent permeability model was established, which accounts for confinement effects, real gas effects, effective pressure, adsorption, surface diffusion, and end effects. Through comparisons with published experimental data and other models, the reliability of the new model was validated.

We found that at low pore pressures, neglecting the real gas effect leads to an overestimation of the apparent permeability, while at high pore pressures, it leads to an underestimation. In addition, neglecting surface diffusion and end effects will result in an underestimation of the actual value, and overlooking effective pressure will lead to an overestimation. At a pore radius of 5 nm, surface diffusion and the real gas effect have the most significant influence, followed by effective pressure, with end effects having the least impact. At a pore radius of 10 nm, surface diffusion and the real gas effect remain predominant, followed by end effects, with effective pressure being the least significant. For pore radii of 25 nm or greater, the influence of end effects is most pronounced, while the impact of surface diffusion and effective pressure is comparable, and the real gas effect is minimal.

It was found that as the ratio of channel length to radius increases, the apparent permeability gradually decreases. Moreover, the apparent permeability decreases with increasing volumetric strain. Under the same pore pressure, the apparent permeability of shale decreases with the increase of the permeability coefficient and the internal swelling coefficient, and increases with the rise of the porosity coefficient. In future work, a shale apparent permeability model based on actual pore structure may be introduced to address the limitations of the present model.

This study employs a capillary model with circular pores, which introduces certain limitations. First, the assumption of uniform circular cross-sections simplifies the complex and heterogeneous pore geometries (e.g., slit-like or irregular shapes) and surface roughness inherent to shale, which can influence flow regimes and the Knudsen layer. Second, the model does not explicitly account for the connectivity of the pore network or the presence of dead-end pores, focusing instead on transport within individual pores. These simplifications may affect the accuracy of predictions under conditions where network effects dominate. Future work should focus on addressing these limitations. Integrating the proposed transport mechanisms into pore-network models or performing simulations on 3D digital rock geometries would allow assessment of pore connectivity and shape effects. Furthermore, systematic experimental validation across a wider range of shale types is needed to better constrain model parameters and verify its broader applicability.

CRediT authorship contribution statement

Shuai Chen: Writing – review & editing, Writing – original draft, Validation, Methodology. **Fu-Shen Liu:** Writing – review & editing. **Feng-Gang Wen:** Writing – review & editing. **Hong-Fei Duan:** Writing – review & editing. **Xu-Lin Peng:** Writing – review & editing.

Data availability

Data will be made available on reasonable request from the corresponding author.

Declaration of competing interest

The authors declare no conflict of interests.

Acknowledgements

This work was funded by Open Foundation of Shaanxi Key Laboratory of Lacustrine Shale Gas Accumulation and Exploitation and the National Natural Science Foundation of China (No. 42577162).

References

Adesida, A.G., Akkutlu, I.Y., Resasco, D.E., et al., 2011. Kerogen pore size distribution of Barnett shale using DFT analysis and Monte Carlo simulations. SPE Annual Technical Conference and Exhibition, Denver, Colorado, USA, October 2011. https://doi.org/10.2118/147397-MS.

Akilu, S., Padmanabhan, E., Sun, Z., 2021. A review of transport mechanisms and models for unconventional tight shale gas reservoir systems. Int. J. Heat Mass Tran. 175, 121125. https://doi.org/10.1016/j.ijheatmasstransfer.2021.121125.

Arif, M., Lebedev, M., Barifcani, A., et al., 2017. Influence of shale-total organic content on CO_2 geo-storage potential. Geophys. Res. Lett. 44, 8769–8775. https://doi.org/10.1002/2017GL073532.

Bartók, A.P., Payne, M.C., Kondor, R., et al., 2010. Gaussian approximation potentials: The accuracy of quantum mechanics, without the electrons. Phys. Rev. Lett. 104 (13), 136403. https://doi.org/10.1103/PhysRevLett.104.136403.

Behler, J., 2016. Perspective: machine learning potentials for atomistic simulations. J. Chem. Phys. 145, 170901. https://doi.org/10.1063/1.4966192.

Beskok, A., Karniadakis, G.E., 1999. A model for flows in channels, pipes, and ducts at micro and nano scales. Microscale Thermophys. Eng. 3 (1), 43–77. https://doi.org/10.1080/108939599199864.

Cai, J.C., Lin, D.L., Singh, H., et al., 2018. Shale gas transport model in 3D fractal porous media with variable pore sizes. Mar. Petrol. Geol. 98, 437–447. https://doi.org/10.1016/j.marpetgeo.2018.08.040.

Cao, P., Liu, J.S., Leong, Y.-K., 2016. General gas permeability model for porous media: Bridging the gaps between conventional and unconventional natural gas reservoirs. Energy Fuels 30, 5492–5505. https://doi.org/10.1021/acs.energyfuels.6b00683.

Chalmers, G.R., Bustin, R.M., Power, I.M., 2012. Characterization of gas shale pore systems by porosimetry, pycnometry, surface area, and field emission scanning electron microscopy/transmission electron microscopy image analyses: Examples from the Barnett, Woodford, Haynesville, Marcellus, and Doig units. AAPG Bull. 96 (6), 1099–1119. https://doi.org/10.1306/10171111052.

Chen, Q., Tang, X., Shi, Y., et al., 2025. Nanomechanics and pore structure evolution in organic-rich shale reservoirs during high-temperature treatment: A multi-scale analysis of microscopic stability. Adv. Geo-Energy Res. 17 (3), 241–255. https://doi.org/10.46690/ager.2025.09.06.

Chen, Y.D., Yang, R.T., 1991. Concentration dependence of surface diffusion and zeolitic diffusion. AIChE J. 37, 1579–1582. https://doi.org/10.1002/aic.690371015.
Choi, J.G., Do, D.D., Do, H.D., 2001. Surface diffusion of adsorbed molecules in porous media: Monolayer, multilayer, and capillary condensation regimes. Ind. Eng. Chem. Res. 40 (19), 4005–4031. https://doi.org/10.1021/ie010195z.
Civan, F., 2010. Effective correlation of apparent gas permeability in tight porous media. Transport Porous Media 82 (2), 375–384. https://doi.org/10.1007/s11242-009-9432-z.
Civan, F., 2019. Stress dependency of permeability represented by an elastic cylindrical pore-shell model: Comment on Zhu et al. (Transp Porous Med (2018) 122: 235–252). Transport Porous Media 127, 573–585. https://doi.org/10.1007/s11242-018-1213-0.
Darabi, H., Ettehad, A., Javadpour, F., et al., 2012. Gas flow in ultra-tight shale strata. J. Fluid Mech. 710, 641–658. https://doi.org/10.1017/jfm.2012.424.
Dong, J.J., Hsu, J.Y., Wu, W.J., et al., 2010. Stress-dependence of the permeability and porosity of sandstone and shale from TCDP Hole-A. Int. J. Rock Mech. Min. 47, 1141–1157. https://doi.org/10.1016/j.ijrmms.2010.06.019.
Duan, Z.P., Muzychka, Y.S., 2007. Slip flow in non-circular microchannels. Microfluid. Nanofluidics 3 (4), 473–484. https://doi.org/10.1007/s10404-006-0141-4.
Gad-el-Hak, M., 2003. Comments on "critical view on new results in micro-fluid mechanics. Int. J. Heat Mass Tran. 46, 3941–3945. https://doi.org/10.1016/S0017-9310(03)00191-1.
Gao, Q., Cheng, Y.F., Han, S.C., et al., 2021a. Coupled hydro-mechanical modeling of gas flow in shale matrix considering the fractal characteristics of nanopores. Fractals 29 (8), 2150266. https://doi.org/10.1142/s0218348x21502662.
Gao, Q., Cheng, Y.F., Han, S.C., et al., 2021b. Fractal analysis of shale gas transport through micropores and microfractures. Fractals 29 (3), 2150068. https://doi.org/10.1142/S0218348X21500687.
Gao, Q., Cheng, Y.F., Han, S.C., et al., 2021c. Effect of shale matrix heterogeneity on gas transport during production: a microscopic investigation. J. Pet. Sci. Eng. 201, 108526. https://doi.org/10.1016/j.petrol.2021.108526.
Gao, Q., Han, S.C., Cheng, Y.F., et al., 2021d. Apparent permeability model for gas transport through micropores and microfractures in shale reservoirs. Fuel 285, 119086. https://doi.org/10.1016/j.fuel.2020.119086.
Gasteiger, J., Zupan, J., 1993. Neural networks in chemistry. Angew Chem. Int. Ed. Engl. 32 (4), 503–527. https://doi.org/10.1002/anie.199305031.
Ghanizadeh, A., Amann-Hildenbrand, A., Gasparik, M., et al., 2014. Experimental study of fluid transport processes in the matrix system of the European organic-rich shales: II. Posidonia Shale (lower Toarcian, northern Germany). Int. J. Coal Geol. 123, 20–33. https://doi.org/10.1016/j.coal.2013.06.009.
Grathoff, G.H., Peltz, M., Enzmann, F., et al., 2016. Porosity and permeability determination of organic-rich posidonia shales based on 3-D analyses by FIB-SEM microscopy. Solid Earth 7, 1145–1156. https://doi.org/10.5194/se-7-1145-2016.
Graur, I.A., Perrier, P., Ghozlani, W., et al., 2009. Measurements of tangential momentum accommodation coefficient for various gases in plane microchannel. Phys. Fluids 21, 102004. https://doi.org/10.1063/1.3253696.
Gu, X., Cole, D.R., Rother, G., et al., 2015. Pores in Marcellus shale: A neutron scattering and FIB-SEM study. Energy Fuels 29, 1295–1308. https://doi.org/10.1021/acs.energyfuels.5b00033.
Hatami, M., Bayless, D., Sarvestani, A., 2020. A model for stress-dependence of apparent permeability in nanopores of shale gas reservoirs. AIChE J. 66, e16541. https://doi.org/10.1002/aic.16541.
Javadpour, F., 2009. Nanopores and apparent permeability of gas flow in mudrocks (shales and siltstone). J. Can. Pet. Technol. 48 (8), 16–21. https://doi.org/10.2118/09-08-16-DA.
Javadpour, F., Fisher, D., Unsworth, M., 2007. Nanoscale gas flow in shale gas sediments. J. Can. Pet. Technol. 46, 55–61. https://doi.org/10.2118/07-10-06.
Javadpour, F., Singh, H., Rabbani, A., et al., 2021. Gas flow models of shale: A review. Energy Fuels 35, 2999–3010. https://doi.org/10.1021/acs.energyfuels.0c04381.
Kazemi, M., Takbiri-Borujeni, A., 2015. An analytical model for shale gas permeability. Int. J. Coal Geol. 146, 188–197. https://doi.org/10.1016/j.coal.2015.05.010.
Klinkenberg, L.J., 1941. The permeability of porous media to liquid and gases. API Drilling and Production Practice, pp. 200–213.
Lee, A.L., Gonzalez, M.H., Eakin, B.E., 1966. The viscosity of natural gases. J. Petrol. Technol. 18 (8), 997–1000. https://doi.org/10.2118/1340-PA.
Li, Z.H., Ripepi, N., Chen, C., 2020. Using pressure pulse decay experiments and a novel multi-physics shale transport model to study the role of Klinkenberg effect and effective pressure on the apparent permeability of shales. J. Pet. Sci. Eng. 189, 107010. https://doi.org/10.1016/j.petrol.2020.107010.
Lu, S.Q., Cheng, Y.P., Li, W., 2016. Model development and analysis of the evolution of coal permeability under different boundary conditions. J. Nat. Gas Sci. Eng. 31, 129–138. https://doi.org/10.1016/j.jngse.2016.02.049.
Ma, G.Q., Shi, J.F., Xiong, H., et al., 2024. Machine learning assisted molecular modeling from biochemistry to petroleum engineering: A review. Geoenergy Sci. Eng. 236, 212770. https://doi.org/10.1016/j.geoen.2024.212770.
Morini, G.L., 2004. Laminar liquid flow through silicon microchannels. J. Fluid Eng. 126 (3), 485–489. https://doi.org/10.1115/1.1760545.
Noé, F., Tkatchenko, A., Müller, K.-R., et al., 2020. Machine learning for molecular simulation. Annu. Rev. Phys. Chem. 71, 361–390. https://doi.org/10.1146/annurev-physchem-042018-052331.
Pan, B., Li, Y.J., Wang, H.Q., et al., 2018. CO_2 and CH_4 wettabilities of organic-rich shale. Energy Fuels 32 (2), 1914–1922. https://doi.org/10.1021/acs.energyfuels.7b01147.
Peng, Y., Liu, J.S., Pan, Z.J., et al., 2018. Evolution of shale apparent permeability under variable boundary conditions. Fuel 215, 46–56. https://doi.org/10.1016/j.fuel.2017.11.024.
Rylander, E., Philip, M.S., Jiang, T.M., et al., 2013. NMR T2 distributions in Eagle Ford shale: Reflections on pore size. In: SPE Unconventional Resources Conference-USA, the Woodlands, Texas, USA, April 2013.
Shen, Y.H., Pang, Y., Shen, Z.Q., et al., 2018. Multiparameter analysis of gas transport phenomena in shale gas reservoirs: Apparent permeability characterization. Sci. Rep. 8, 2601. https://doi.org/10.1038/s41598-018-20949-2.
Shi, J.Q., Durucan, S., 2004. Drawdown Induced Changes in Permeability of Coalbeds: A New Interpretation of the Reservoir Response to Primary Recovery, vol. 56. Transp. Porous Media, pp. 1–16. https://doi.org/10.1023/B:TIPM.0000018398.19928.5a.
Si, L.L., Li, Z.H., Yang, Y.L., 2018. Influence of the pore geometry structure on the evolution of gas permeability. Transport Porous Media 123, 321–339. https://doi.org/10.1007/s11242-018-1044-z.
Si, L.L., Li, Z.H., Yang, Y.L., 2019. Evolution characteristics of gas permeability under multiple factors. Transport Porous Media 127, 415–432. https://doi.org/10.1007/s11242-018-1199-7.
Sisan, T.B., Lichter, S., 2011. The end of nanochannels. Microfluid. Nanofluidics 11, 787–791. https://doi.org/10.1007/s10404-011-0855-9.
Song, H.S., Li, B.B., Tang, C.L., et al., 2025. Helium diffusion experiments in effective helium source rocks: A case study involving coal, shale, and granite. Gas Sci. Eng. 142, 205688. https://doi.org/10.1016/j.jgsce.2025.205688.
Sparreboom, W., Berg, A.V.D., Eijkel, J.C.T., 2009. Principles and applications of nanofluidic transport. Nat. Nanotechnol. 4 (11), 713–720. https://doi.org/10.1038/nnano.2009.332.
Sun, Z., Shi, J.T., Wu, K.L., et al., 2018. Gas flow behavior through inorganic nanopores in shale considering confinement effect and moisture content. Ind. Eng. Chem. Res. 57, 3430–3440. https://doi.org/10.1021/acs.iecr.8b00271.
Tan, Y.L., Pan, Z.J., Liu, J.S., et al., 2018. Experimental study of impact of anisotropy and heterogeneity on gas flow in coal. Part II: Permeability. Fuel 230, 397–409. https://doi.org/10.1016/j.fuel.2018.05.173.
Tian, W., Wu, X.R., Liu, D.H., et al., 2019. Investigating effects of pore size distribution and pore shape on radon production in marcellus shale gas formation. Energy Fuels 33, 700–707. https://doi.org/10.1021/acs.energyfuels.8b03311.
Velioglu, S., Keskin, S., 2019. Simulation of H_2/CH_4 mixture permeation through MOF membranes using non-equilibrium molecular dynamics. J. Mater. Chem. A 7, 2301–2314. https://doi.org/10.1039/c8ta10167a.
Wang, J., Olsson, S., Wehmeyer, C., et al., 2019. Machine learning of coarse-grained molecular dynamics force fields. ACS Cent. Sci. 5, 755–767. https://doi.org/10.48550/arXiv.1812.01736.
Wang, J.G., Hu, B.W., Liu, H., et al., 2018a. Effects of 'soft–hard' compaction and multiscale flow on the shale gas production from a multistage hydraulic fractured horizontal well. J. Pet. Sci. Eng. 170, 873–887. https://doi.org/10.1016/j.petrol.2018.07.012.
Wang, S., Shi, J.T., Wang, K., et al., 2018b. Apparent permeability model for gas transport in shale reservoirs with nano-scale porous media. J. Nat. Gas Sci. Eng. 55, 508–519. https://doi.org/10.1016/j.jngse.2018.05.026.
Wang, Y.H., Ribeiro, J.M.L., Tiwary, P., 2020. Machine learning approaches for analyzing and enhancing molecular dynamics simulations. Curr. Opin. Struct. Biol. 61, 139–145. https://doi.org/10.1016/j.sbi.2019.12.016.
Watari, M., 2010. Relationship between accuracy and number of velocity particles of the finite-difference lattice Boltzmann method in velocity slip simulations. J. Fluid Eng. 132 (10), 101401. https://doi.org/10.1115/1.4002359.
Weissberg, H.L., 1962. End correction for slow viscous flow through long tubes. Phys. Fluids 5, 1033–1036. https://doi.org/10.1063/1.1724469.
Wu, K.L., Chen, Z.X., Li, X.F., et al., 2015a. Real gas transport through nanopores of varying cross-section type and shape in shale gas reservoirs. Chem. Eng. J. 281, 813–825. https://doi.org/10.1016/j.cej.2015.07.012.
Wu, K.L., Chen, Z.X., Li, X.F., et al., 2016. A model for multiple transport mechanisms through nanopores of shale gas reservoirs with real gas effect-adsorption-mechanic coupling. Int. J. Heat Mass Tran. 93, 408–426. https://doi.org/10.1016/j.ijheatmasstransfer.2015.10.003.
Wu, K.L., Chen, Z.X., Li, X.F., et al., 2017. Flow behavior of gas confined in nanoporous shale at high pressure: Real gas effect. Fuel 205, 173–183. https://doi.org/10.1016/j.fuel.2017.05.055.
Wu, K.L., Li, X.F., Wang, C.C., et al., 2015b. Model for surface diffusion of adsorbed gas in nanopores of shale gas reservoirs. Ind. Eng. Chem. Res. 54, 3225–3236. https://doi.org/10.1021/ie504030v.
Xiong, H., Devegowda, D., Huang, L., 2020. Water bridges in clay nanopores: Mechanisms of formation and impact on hydrocarbon transport. Langmuir 36 (3), 723–733. https://doi.org/10.1021/acs.langmuir.9b03244.

Yu, H., Chen, J., Zhu, Y.B., et al., 2017. Multiscale transport mechanism of shale gas in micro/nano-pores. Int. J. Heat Mass Tran. 111, 1172–1180. https://doi.org/10.1016/j.ijheatmasstransfer.2017.04.050.

Yu, H., Fan, J.C., Chen, J., et al., 2018. Pressure-dependent transport characteristic of methane gas in slit nanopores. Int. J. Heat Mass Tran. 123, 657–667. https://doi.org/10.1016/j.ijheatmasstransfer.2018.03.003.

Yu, H., Zhu, Y.B., Jin, X., et al., 2019. Multiscale simulations of shale gas transport in micro/nano-porous shale matrix considering pore structure influence. J. Nat. Gas Sci. Eng. 64, 28–40. https://doi.org/10.1016/j.jngse.2019.01.016.

Zeng, F.H., Peng, F., Guo, J.C., et al., 2019. Gas mass transport model for micro-fractures considering the dynamic variation of width in shale reservoirs. SPE Reservoir Eval. Eng. 22 (4), 1265–1281. https://doi.org/10.2118/194494-PA.

Zhang, L.H., Liang, H.B., Zhao, Y.L., et al., 2020. Gas transport characteristics in shale matrix based on multiple mechanisms. Chem. Eng. J. 386, 124002. https://doi.org/10.1016/j.cej.2019.124002.

Zhong, X.L., MacCormack, R.W., Chapman, D.R., 1993. Stabilization of the Burnett equations and application to hypersonic flows. AIAA J. 31, 1036–1043. https://doi.org/10.2514/3.11726.

Zhu, H., Qi, B., Li, J., et al., 2025. Unlocking the shiny surface features of shale shear fractures at micro-nanoscale. Adv. Geo-Energy Res. 18 (2), 202–206. https://doi.org/10.46690/ager.2025.11.10.

Zhu, S.Y., Du, Z.M., Li, C.L., et al., 2018. A semi-analytical model for pressure-dependent permeability of tight sandstone reservoirs. Transport Porous Media 122, 235–252. https://doi.org/10.1007/s11242-018-1001-x.